Optimization of the PML Efficiency in 3-D TLM Method

Jean-Lou Dubard and Dominique Pompei

***Abstract*—In this paper, the complete derivation of the new perfectly matched layer symmetrical condensed node (PML SCN) recently proposed for the implementation of the Berenger's PML's in the three-dimensional transmission-line matrix (TLM) method is given. Several comparisons between TLM and finite-difference time-domain experiments are performed in order to better understand the behavior of PML's in TLM simulations. In particular, the way to implement the numerical conductivity values with the PML SCN is considered. TLM simulations of waveguide and microstrip antennas are finally presented to prove that the use of this new PML SCN improves the absorbing boundary conditions in the TLM.**

***Index Terms*—Absorbing boundary, perfectly matched layer, TLM method.**

I. Introduction

PERFECTLY matched layers (PML's) are layers especially designed by Berenger [1] to simulate free space at the boundaries of a finite-difference time-domain (FDTD) computational domain. The PML was first implemented in the transmission-line matrix (TLM) [2], [3] method using an interface between the FDTD and the TLM network. However, it was shown that the use of a nonuniform TLM–FDTD mesh provides more inaccurate absorbing conditions than obtained by Berenger with the FDTD method. A uniform type of a two-dimensional (2-D) TLM mesh, which can simulate usual and PML media at once, was then developed in [4] and, recently, we have proposed a new symmetrical condensed node (SCN) for the implementation of the Berenger's PML's in a three-dimensional (3-D) TLM method [5]. Two other types of 3-D PML–TLM nodes were developed at the same time by other authors [6], [7]. They are, however, different from the one presented in [5], as there are many degrees of freedom to built a PML–TLM node. It was shown in [5] that a PML implemented with this modified node provides 30 dB more accurate boundary conditions than Higdon's conditions and matched termination. We propose here to give a complete derivation of this new PML SCN from Maxwell's equations in PML media and to provide additional evaluations of the PML efficiency by performing comparisons between the TLM and FDTD methods. From these comparisons, the optimal way to implement the numerical conductivity values in the new PML symmetrical condensed node will be given. It will then be shown that the numerical behavior of the PML in TLM simulations is very close to the one observed by Berenger in FDTD experiments. In the last section of this paper, PML's will be used to simulate the wave propagation on an infinite waveguide and to calculate the radiating properties of a microstrip antenna.

Manuscript received June 30, 1998. This work was supported by the Centre National de Calcul Parallele en Sciences de la Terre, the Institut du Développement et des Ressources en Informatique Scientifique, and the Centre National Universitaire Sud de Calcul.

The authors are with the Laboratoire d'Electronique, Antennes et Télécommunications, Université de Nice-Sophia Antipolis, 06560 Valbonne, France (e-mail: jdubard@elec.unice.fr).

Publisher Item Identifier S 0018-9480(00)05467-3.

II. Derivation of the PML SCN

PML media are described by modifying Maxwell equations with the six electromagnetic-field components split into 12 subcomponents and with anisotropic electric and magnetic conductivities [8]. For example, in a usual media with isotropic electric conductivity σ, the first Maxwell's equation can be written as follows:

$$\varepsilon_0\varepsilon_r\frac{\partial e_x}{\partial t}+\sigma e_x=\frac{\partial h_z}{\partial y}-\frac{\partial h_y}{\partial z}. \tag{1}$$

In Berenger's PML media, each electromagnetic field is split into two subcomponents

$$e_x=e_{xy}+e_{xz}\quad h_y=h_{yx}+h_{yz}\quad h_z=h_{zx}+h_{zy} \tag{2}$$

and (1) is replaced by

$$\begin{aligned}\varepsilon_0\varepsilon_r\frac{\partial e_{xy}}{\partial t}+\sigma_y e_{xy}&=\frac{\partial(h_{zx}+h_{zy})}{\partial y}\\ \varepsilon_0\varepsilon_r\frac{\partial e_{xz}}{\partial t}+\sigma_z e_{xz}&=-\frac{\partial(h_{yx}+h_{yz})}{\partial z}\end{aligned} \tag{3}$$

where σ_y and σ_z are the electric conductivities along the y- and z-axes. Equation (3) can be rewritten in the following forms:

$$\begin{aligned}\varepsilon_0\varepsilon_r\frac{\partial(e_x-e_{xz})}{\partial t}+\sigma_y e_{xy}&=\frac{\partial h_z}{\partial y}\\ \varepsilon_0\varepsilon_r\frac{\partial(e_x-e_{xy})}{\partial t}+\sigma_z e_{xz}&=-\frac{\partial h_y}{\partial z}\end{aligned} \tag{4}$$

or

$$\begin{aligned}\frac{Y_x+4}{2}\frac{\partial E_x}{\partial T}&=\frac{\partial H_z}{\partial Y}+\frac{Y_x+4}{2}\frac{\partial E_{xz}}{\partial T}-G_{xy}E_{xy}\\ \frac{Y_x+4}{2}\frac{\partial E_x}{\partial T}&=\frac{\partial H_y}{\partial Z}+\frac{Y_x+4}{2}\frac{\partial E_{xy}}{\partial T}-G_{xz}E_{xz}\end{aligned} \tag{5}$$

using

$$X=\frac{x}{u}$$
$$Y=\frac{y}{v}$$

$$
\begin{aligned}
Z &= \frac{z}{w} \\
T &= \frac{t}{\Delta t} \\
E_x &= e_x u \\
E_{xy} &= e_{xy} u \\
E_{xz} &= e_{xz} u \\
H_y &= h_y v Z_0 \\
H_z &= h_z w Z_0 \\
Y_x &= 4\left(\varepsilon_r \frac{vw}{u\Delta l} - 1\right) \\
G_{xy} &= \sigma_y \frac{vw}{u} Z_0 \\
G_{xz} &= \sigma_z \frac{vw}{u} Z_0
\end{aligned} \tag{6}
$$

where u, v, and w are the sizes of the TLM SCN shown in Fig. 1. The node is located in the TLM network by indexes (i, j, k). Δl is the smallest cell size over the network and the time step is set as $\Delta t \leq \Delta l/2c$. Z_0 and c are the characteristic impedance and the wave velocity of free space, respectively.

As described by Jin *et al.* [9], (5) is reformulated as

$$
\frac{1}{2}\left\{\frac{\partial(E_x - H_z)}{\partial A_y} - \frac{\partial(E_x + H_z)}{\partial B_y}\right\} = \frac{\partial E_{xz}}{\partial T} - \frac{Y_x + 2}{2}\frac{\partial E_{xy}}{\partial T} - G_{xy}E_{xy} \tag{7a}
$$

$$
\frac{1}{2}\left\{\frac{\partial(E_x + H_y)}{\partial A_z} - \frac{\partial(E_x - H_y)}{\partial B_z}\right\} = \frac{\partial E_{xy}}{\partial T} - \frac{Y_x + 2}{2}\frac{\partial E_{xz}}{\partial T} - G_{xz}E_{xz} \tag{7b}
$$

using the following new coordinate system where time and space are mixed:

$$
\begin{aligned}
A_x &= X + T \\
A_y &= Y + T \\
A_z &= Z + T \\
B_x &= X - T \\
B_y &= Y - T \\
B_z &= Z - T.
\end{aligned} \tag{8}
$$

A set of finite-difference equations can be obtained from (7) by using centered differencing at point (i, j, k) and time $n\Delta t$ in the new coordinate system (8). For example, (7a) gives

$$
\begin{aligned}
&\frac{1}{2}\left[E_x\left(n+\frac{1}{2}, i, j+\frac{1}{2}, k\right) - H_z\left(n+\frac{1}{2}, i, j+\frac{1}{2}, k\right)\right] \\
&-\frac{1}{2}\left[E_x\left(n-\frac{1}{2}, i, j-\frac{1}{2}, k\right) - H_z\left(n-\frac{1}{2}, i, j-\frac{1}{2}, k\right)\right] \\
&-\frac{1}{2}\left[E_x\left(n-\frac{1}{2}, i, j+\frac{1}{2}, k\right) + H_z\left(n-\frac{1}{2}, i, j+\frac{1}{2}, k\right)\right] \\
&+\frac{1}{2}\left[E_x\left(n+\frac{1}{2}, i, j-\frac{1}{2}, k\right) + H_z\left(n+\frac{1}{2}, i, j-\frac{1}{2}, k\right)\right]
\end{aligned}
$$

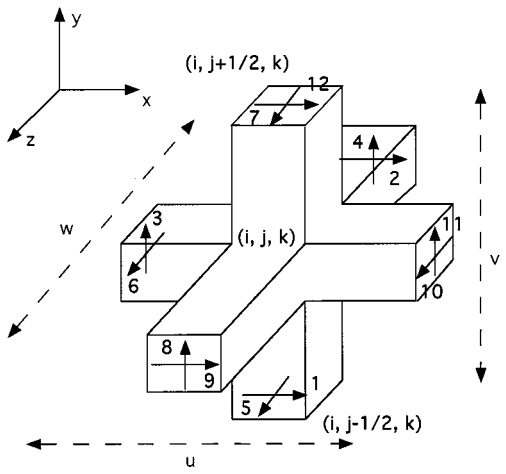

Fig. 1. TLM SCN.

$$
\begin{aligned}
&+\frac{Y_x+2}{2}\left[E_{xy}\left(n+\frac{1}{2}, i, j, k\right) - E_{xy}\left(n-\frac{1}{2}, i, j, k\right)\right] \\
&-\left[E_{xz}\left(n+\frac{1}{2}, i, j, k\right) - E_{xz}\left(n-\frac{1}{2}, i, j, k\right)\right] \\
&+G_{xy}E_{xy}(n, i, j, k) = 0.
\end{aligned} \tag{9}
$$

In TLM formulation, each elementary plane waves penetrating into the cell along the x-, y-, and z-directions of space is associated with a voltage impulse travelling toward the center of the cell through one of the 12 transmission lines linking the node to its six neighbors. For example, an x-polarized plane wave propagating in the $+y$-direction is related to the incident voltage impulse ${}_nV_1^i$ on port number 1 at the cell boundary $(i, j-1/2, k)$ and time step $(n-1/2)\Delta t$ as follows:

$$
E_x\left(n-\frac{1}{2}, i, j-\frac{1}{2}, k\right) - H_z\left(n-\frac{1}{2}, i, j-\frac{1}{2}, k\right) = 2_nV_1^i. \tag{10a}
$$

According to the Huygens' principle, these incident voltage impulses are scattered at the center of the node and at time step $n\Delta t$ into reflected voltage impulses associated with outgoing plane waves. For example, for an x-polarized outgoing wave propagating in the $+y$-direction, the relation between the E_x- and H_z-field components and the reflected voltage impulse ${}_nV_{12}^r$ on port number 12 at the cell boundary $(i, j+1/2, k)$ and time step $(n+1/2)\Delta t$ is

$$
E_x\left(n+\frac{1}{2}, i, j+\frac{1}{2}, k\right) - H_z\left(n+\frac{1}{2}, i, j+\frac{1}{2}, k\right) = 2_nV_{12}^r. \tag{10b}
$$

Open and short stubs connected at the center of the node allow to model the permittivity and permeability of various materials. In the case of x-polarized waves, for example, it is necessary to add two open stubs with normalized characteristic admittance Y_x (numbered 13 and 14), to take into account the two subcomponents E_{xy} and E_{xz} as follows:

$$
\begin{aligned}
E_{xy}\left(n-\frac{1}{2}, i, j, k\right) &= 2_nV_{13}^i \\
E_{xz}\left(n-\frac{1}{2}, i, j, k\right) &= 2_nv_{14}^i
\end{aligned} \tag{10c}
$$

and

$$E_{xy}\left(n+\frac{1}{2},\, i,\, j,\, k\right) = 2_nV_{13}^r$$
$$E_{xz}\left(n+\frac{1}{2},\, i,\, j,\, k\right) = 2_nv_{14}^r. \tag{10d}$$

Using (10a)–(10d), (9) can be reduced to

$$\begin{aligned}{}_nV_1^r + {}_nV_{12}^r - {}_nV_1^i - {}_nV_{12}^i + (Y_x+2)\left({}_nV_{13}^r - {}_nV_{13}^i\right)\\ -2\left({}_nV_{14}^r - {}_nV_{14}^i\right) + G_{xy}E_{xy}(n,\, i,\, j,\, k) = 0.\end{aligned} \tag{11}$$

Another set of finite-difference equations can be obtained from (3), which can be rewritten using (2) and (6) as

$$\frac{Y_x+4}{2}\,\frac{\partial E_{xy}}{\partial T} = \frac{\partial H_z}{\partial Y} - G_{xy}E_{xy} \tag{12a}$$

$$\frac{Y_x+4}{2}\,\frac{\partial E_{xz}}{\partial T} = \frac{\partial H_y}{\partial Z} - G_{xz}E_{xz}. \tag{12b}$$

By using centered differencing and averaging at point (i, j, k) and time step $(n+1/2)\Delta t$ in the coordinate system (6), and by using (10a)–(10d), (12a), for example, gives

$$\begin{aligned}&\frac{Y_x+G_{xy}+4}{2}\left[E_{xy}(n+1,\, i,\, j,\, k) - E_{xy}(n,\, i,\, j,\, k)\right]\\ &\quad = {}_{n+1}V_1^i + {}_{n+1}V_{12}^i - {}_nV_1^r - {}_nV_{12}^r - G_{xy}E_{xy}(n,\, i,\, j,\, k).\end{aligned} \tag{13}$$

Substituting (11) into (13), we obtain finally

$$E_{xy}(n,\, i,\, j,\, k) = \frac{2\left({}_nV_1^i + {}_nV_{12}^i + (Y_x+2){}_nV_{13}^i - 2_nV_{14}^i\right)}{Y_x+G_{xy}+4}. \tag{14a}$$

Performing the same procedure for the other 11 modified Maxwell equations provide the following expressions:

$$\begin{aligned}&E_{xz}(n,\, i,\, j,\, k)\\ &\quad = \frac{2\left({}_nV_2^i + {}_nV_9^i + (Y_x+2){}_nV_{14}^i - 2_nV_{13}^i\right)}{Y_x+G_{xz}+4}\end{aligned} \tag{14b}$$

$$\begin{aligned}&E_{yx}(n,\, i,\, j,\, k)\\ &\quad = \frac{2\left({}_nV_3^i + {}_nV_{11}^i + (Y_y+2){}_nV_{15}^i - 2_nV_{16}^i\right)}{Y_y+G_{yx}+4}\end{aligned} \tag{14c}$$

$$\begin{aligned}&E_{yz}(n,\, i,\, j,\, k)\\ &\quad = \frac{2\left({}_nV_4^i + {}_nV_8^i + (Y_y+2){}_nV_{16}^i - 2_nV_{15}^i\right)}{Y_y+G_{yz}+4}\end{aligned} \tag{14d}$$

$$\begin{aligned}&E_{zx}(n,\, i,\, j,\, k)\\ &\quad = \frac{2\left({}_nV_6^i + {}_nV_{10}^i + (Y_z+2){}_nV_{17}^i - 2_nV_{18}^i\right)}{Y_z+G_{zx}+4}\end{aligned} \tag{14e}$$

$$\begin{aligned}&E_{zy}(n,\, i,\, j,\, k)\\ &\quad = \frac{2\left({}_nV_5^i + {}_nV_7^i + (Y_z+2){}_nV_{18}^i - 2_nV_{17}^i\right)}{Y_z+G_{zy}+4}\end{aligned} \tag{14f}$$

$$\begin{aligned}&H_{xy}(n,\, i,\, j,\, k)\\ &\quad = \frac{2\left({}_nV_5^i - {}_nV_7^i + \left(1+\frac{2}{Z_x}\right){}_nV_{19}^i - \frac{2}{Z_x}{}_nV_{20}^i\right)}{Z_x+R_{xy}+4}\end{aligned} \tag{14g}$$

$$\begin{aligned}&H_{xz}(n,\, i,\, j,\, k)\\ &\quad = \frac{2\left({}_nV_8^i - {}_nV_4^i + \left(1+\frac{2}{Z_x}\right){}_nV_{20}^i - \frac{2}{Z_x}{}_nV_{19}^i\right)}{Z_x+R_{xz}+4}\end{aligned} \tag{14h}$$

$$\begin{aligned}&H_{yx}(n,\, i,\, j,\, k)\\ &\quad = \frac{2\left({}_nV_{10}^i - {}_nV_6^i + \left(1+\frac{2}{Z_y}\right){}_nV_{21}^i - \frac{2}{Z_y}{}_nV_{22}^i\right)}{Z_y+R_{yx}+4}\end{aligned} \tag{14i}$$

$$\begin{aligned}&H_{yz}(n,\, i,\, j,\, k)\\ &\quad = \frac{2\left({}_nV_2^i - {}_nV_9^i + \left(1+\frac{2}{Z_y}\right){}_nV_{22}^i - \frac{2}{Z_y}{}_nV_{21}^i\right)}{Z_y+R_{yz}+4}\end{aligned} \tag{14j}$$

$$\begin{aligned}&H_{zx}(n,\, i,\, j,\, k)\\ &\quad = \frac{2\left({}_nV_3^i - {}_nV_{11}^i + \left(1+\frac{2}{Z_z}\right){}_nV_{23}^i - \frac{2}{Z_z}{}_nV_{24}^i\right)}{Z_z+R_{zx}+4}\end{aligned} \tag{14k}$$

$$\begin{aligned}&H_{zy}(n,\, i,\, j,\, k)\\ &\quad = \frac{2\left({}_nV_{12}^i - {}_nV_1^i + \left(1+\frac{2}{Z_z}\right){}_nV_{24}^i - \frac{2}{Z_z}{}_nV_{23}^i\right)}{Z_z+R_{zy}+4}\end{aligned} \tag{14l}$$

where

$$Y_x = 4\left(\varepsilon_r\frac{vw}{u\Delta l} - 1\right)$$
$$Y_y = 4\left(\varepsilon_r\frac{uw}{v\Delta l} - 1\right)$$
$$Y_z = 4\left(\varepsilon_r\frac{uv}{w\Delta l} - 1\right)$$

$$
\begin{aligned}
Z_x &= 4\left(\mu_r \frac{vw}{u\Delta l} - 1\right)\\
Z_y &= 4\left(\mu_r \frac{uw}{v\Delta l} - 1\right)\\
Z_z &= 4\left(\mu_r \frac{uv}{w\Delta l} - 1\right)\\
G_{xy} &= \sigma_y Z_o \frac{vw}{u}\\
G_{yz} &= \sigma_z Z_o \frac{uw}{v}\\
G_{zx} &= \sigma_x Z_o \frac{uv}{w}\\
G_{xz} &= \sigma_z Z_o \frac{vw}{u}\\
G_{yx} &= \sigma_x Z_o \frac{uw}{v}\\
G_{zy} &= \sigma_y Z_o \frac{uv}{w}\\
R_{xy} &= \sigma_y^* Z_o^{-1} \frac{vw}{u}\\
R_{yz} &= \sigma_z^* Z_o^{-1} \frac{uw}{v}\\
R_{zx} &= \sigma_x^* Z_o^{-1} \frac{uv}{w}\\
R_{xz} &= \sigma_z^* Z_o^{-1} \frac{vw}{u}\\
R_{yx} &= \sigma_x^* Z_o^{-1} \frac{uw}{v}\\
R_{zy} &= \sigma_y^* Z_o^{-1} \frac{uv}{w}.
\end{aligned} \tag{15}
$$

In (15), σ_x^*, σ_y^*, and σ_z^* are the magnetic conductivities along the x-, y-, and z-axes. Note that, to prevent the term in $1/Z$ to go to infinity in (14g)–(14l) when $u = v = w = \Delta l$ and $\mu_r = 1$, it is necessary to take Δt slightly lower than the maximum time step $\Delta l/2c$. Futhermore, in the case of usual media with isotropic electric and magnetic conductivities σ and σ^*, (14a) and (14b) can be reduced to

$$
\begin{aligned}
E_x &= E_{xy} + E_{xz}\\
&= \frac{2\left({}_nV_1^i + {}_nV_{12}^i + {}_nV_2^i + {}_nV_9^i + Y_x({}_nV_{13}^i + {}_nV_{14}^i)\right)}{Y_x + G_x + 4}
\end{aligned} \tag{16}
$$

where $G_x = G_{xy} = G_{xz}$. Equation (16) is the E_x-field expression for the standard SCN. This new PML SCN can then simulate at once PML layers and the usual media as vacuum or conductive media. It can be used in all the computational domain leading to a uniform algorithm.

As described in [9], the scattering process can finally be obtained by using averaging in space-time coordinate system (8) from field expressions $E_a \pm H_b$, where superscript a and b are x, y, or z. The 24×24 scattering matrix of this new PML SCN has already been given in [5] and can be formulated as follows for a practical point-of-view of computation:

$$
\begin{aligned}
{}_nV_1^r &= \left[E_{xy}(n,i,j,k) + E_{xz}(n,i,j,k)\right]\\
&\quad + \left[H_{zx}(n,i,j,k) + H_{zy}(n,i,j,k)\right] - {}_nV_{12}^i\\
{}_nV_2^r &= \left[E_{xy}(n,i,j,k) + E_{xz}(n,i,j,k)\right]\\
&\quad - \left[H_{yx}(n,i,j,k) + H_{yz}(n,i,j,k)\right] - {}_nV_9^i\\
{}_nV_3^r &= \left[E_{yx}(n,i,j,k) + E_{yz}(n,i,j,k)\right]\\
&\quad - \left[H_{zx}(n,i,j,k) + H_{zy}(n,i,j,k)\right] - {}_nV_{11}^i\\
{}_nV_4^r &= \left[E_{yx}(n,i,j,k) + E_{yz}(n,i,j,k)\right]\\
&\quad + \left[H_{xy}(n,i,j,k) + H_{xz}(n,i,j,k)\right] - {}_nV_8^i\\
{}_nV_5^r &= \left[E_{zx}(n,i,j,k) + E_{zy}(n,i,j,k)\right]\\
&\quad - \left[H_{xy}(n,i,j,k) + H_{xz}(n,i,j,k)\right] - {}_nV_7^i\\
{}_nV_6^r &= \left[E_{zx}(n,i,j,k) + E_{zy}(n,i,j,k)\right]\\
&\quad + \left[H_{yx}(n,i,j,k) + H_{yz}(n,i,j,k)\right] - {}_nV_{10}^i\\
{}_nV_7^r &= \left[E_{zx}(n,i,j,k) + E_{zy}(n,i,j,k)\right]\\
&\quad + \left[H_{xy}(n,i,j,k) + H_{xz}(n,i,j,k)\right] - {}_nV_5^i\\
{}_nV_8^r &= \left[E_{yx}(n,i,j,k) + E_{yz}(n,i,j,k)\right]\\
&\quad - \left[H_{xy}(n,i,j,k) + H_{xz}(n,i,j,k)\right] - {}_nV_4^i\\
{}_nV_9^r &= \left[E_{xy}(n,i,j,k) + E_{xz}(n,i,j,k)\right]\\
&\quad + \left[H_{yx}(n,i,j,k) + H_{yz}(n,i,j,k)\right] - {}_nV_2^i\\
{}_nV_{10}^r &= \left[E_{zx}(n,i,j,k) + E_{zy}(n,i,j,k)\right]\\
&\quad - \left[H_{yx}(n,i,j,k) + H_{yz}(n,i,j,k)\right] - {}_nV_6^i\\
{}_nV_{11}^r &= \left[E_{yx}(n,i,j,k) + E_{yz}(n,i,j,k)\right]\\
&\quad + \left[H_{zx}(n,i,j,k) + H_{zy}(n,i,j,k)\right] - {}_nV_3^i\\
{}_nV_{12}^r &= \left[E_{xy}(n,i,j,k) + E_{xz}(n,i,j,k)\right]\\
&\quad - \left[H_{zx}(n,i,j,k) + H_{zy}(n,i,j,k)\right] - {}_nV_1^i\\
{}_nV_{13}^r &= E_{xy}(n,i,j,k) - {}_nV_{13}^i\\
{}_nV_{14}^r &= E_{xz}(n,i,j,k) - {}_nV_{14}^i\\
{}_nV_{15}^r &= E_{yx}(n,i,j,k) - {}_nV_{15}^i\\
{}_nV_{16}^r &= E_{yz}(n,i,j,k) - {}_nV_{16}^i\\
{}_nV_{17}^r &= E_{zx}(n,i,j,k) - {}_nV_{17}^i\\
{}_nV_{18}^r &= E_{zy}(n,i,j,k) - {}_nV_{18}^i\\
{}_nV_{19}^r &= {}_nV_{19}^i - Z_x H_{xy}(n,i,j,k)\\
{}_nV_{20}^r &= {}_nV_{20}^i - Z_x H_{xz}(n,i,j,k)\\
{}_nV_{21}^r &= {}_nV_{21}^i - Z_y H_{yx}(n,i,j,k)\\
{}_nV_{22}^r &= {}_nV_{22}^i - Z_y H_{yz}(n,i,j,k)\\
{}_nV_{23}^r &= {}_nV_{23}^i - Z_z H_{zx}(n,i,j,k)\\
{}_nV_{24}^r &= {}_nV_{24}^i - Z_z H_{zy}(n,i,j,k).
\end{aligned} \tag{17}
$$

Then, scattering with the PML SCN requires 108 additions/substractions, 42 multiplications, and 12 divisions in place of 54 additions/substractions and 12 multiplications with the standard SCN. This higher computational cost may be prohibitive. Thus, it is recommended to use the standard SCN in the domain of interest and the PML SCN in the PML layers. This can be done without difficulties. Since the 12-link lines are the same for the two nodes, they can be directly connected together at the interface vacuum–PML medium.

III. Comparisons Between TLM and FDTD Methods

We have presented in [5] some numerical results that have proven the ability of the PML SCN to absorb outgoing waves. Nevertheless, the numerical behavior of the PML layers has

been studied intensively in FDTD simulations. To better evaluate the efficiency of the new PML SCN, additional TLM simulations were then performed and compared to the results obtained with the FDTD method.

A. Efficiency of the PML with a Parabolic Conductivity Profile

We have first considered the well-known benchmark test constituted by a simple point source radiating in a free space of $51 \times 51 \times 51$ cells, as in [10]. This computational domain is surrounded by PML layers. Ez at the center of the domain is excited with a smooth compact pulse and the response at time-step 100 is observed along the line $(i, 1, 1)$ where $i = 1$–51. This response is compared to a reference solution obtained with a large domain of $151 \times 151 \times 151$ cells by computing the local error

$$\text{error}(i) = \left|E_z(i,\,1,\,1) - E_{z\,\text{ref}}(i,\,1,\,1)\right|, \qquad \text{for } i = 1,\,51. \tag{18}$$

PML layers used to troncate the computational domain are denoted PML(N–P–R). N is the number of cells in the layer and R is the theoretical reflection factor expressed in percentage. P means that the conductivity increases in the layer as a parabolic progression. In a FDTD algorithm, such numerical conductivities are implemented [11] using averaging in the cell around the index location L as follows:

$$\begin{aligned}\sigma(0) &= -\frac{\varepsilon_0 c}{2^4}\,\frac{Ln(R)}{\Delta l N^3}\\ \sigma(L) &= \sigma(0)\Big[(2L+1)^3 - (2L-1)^3\Big],\\ &\qquad \text{for } L = \frac{1}{2},\,1,\,\frac{3}{2},\,2,\,\cdots,\,N-\frac{1}{2}.\end{aligned} \tag{19}$$

In (19), $\sigma(0)$ is the numerical conductivity at the interface between the last cell in the vacuum and the first cell in the PML. Due to the shift $\Delta l/2$ between the electric- and magnetic-field component in the Yee cell, the numerical conductivities σ and σ^* are not implemented at the same index location L. In the TLM scheme, a parabolic conductivity profile can be implemented using (19), except that the numerical conductivities σ and σ^* are located at the same index location $L = 1, 2, \cdots, N-1$. However, although the numerical conductivities σ are the same for both methods, the ratio of conductivity is different. In the FDTD, the ratio of conductivity from one index location to the next decreases as follows:

$$\begin{aligned}\frac{\sigma(1/2)}{\sigma(0)} &= 8\\ \frac{\sigma(1)}{\sigma(1/2)} &= 3.25\\ \frac{\sigma(3/2)}{\sigma(1)} &= 2.15,\,\cdots\\ \frac{\sigma(L+1/2)}{\sigma(L)} &= \frac{(2L+2)^3 - (2L)^3}{(2L+1)^3 - (2L-1)^3}\end{aligned} \tag{20}$$

while in TLM, we have

$$\begin{aligned}\frac{\sigma(1)}{\sigma(0)} &= 26\\ \frac{\sigma(2)}{\sigma(1)} &= 3.77\\ \frac{\sigma(3)}{\sigma(2)} &= 2.22\\ \frac{\sigma(L+1)}{\sigma(L)} &= \frac{(2L+3)^3 - (2L+1)^3}{(2L+1)^3 - (2L-1)^3}.\end{aligned} \tag{21}$$

The PML with a higher conductivity ratio gives more numerical reflections, as reported by Berenger in [11]. Consequently, the numerical errors computed with the TLM method are 20 dB higher than those obtained in [10] with the FDTD method. To obtain better results in the TLM, it is necessary to reduce the conductivity ratio for the first two cells in the PML. This can be done by implementing parabolic conductivity profile using the following expressions:

$$\begin{aligned}\sigma(0) &= -\frac{\varepsilon_0 c}{2}\,\frac{Ln(R)}{\Delta l N^3}\\ \sigma(L) &= \sigma(0)\Big[(L+1)^3 - (L)^3\Big], \qquad \text{for } L = 1,\,2,\,\cdots,\,N-1.\end{aligned} \tag{22}$$

Now the conductivity ratio varies approximately as in the FDTD since $\sigma(1)/\sigma(0) = 7$. However, the numerical conductivity $\sigma(0)$ increases by a factor of eight, leading still to high numerical reflections, as predicted by Berenger. To obtain the same numerical conductivity $\sigma(0)$ in the TLM as in the FDTD, it is necessary to increase N or R. In order to not increase the computational cost, it is recommended to modify R rather than N. Since higher values of R mean lower values of $\sigma_{\max}$ at the end of the PML, the PML needs to be backed by matched terminations in TLM simulations rather than perfectly conducting conditions as used in the FDTD method. Then, with such conditions, PML's provide as good absorption in the TLM as in FDTD simulations, as observed in Fig. 2. Nevertheless, especially for thinner layers, it seems to be necessary to add one cell to the PML to obtain as good of a performance in the TLM as in the FDTD method.

B. Efficiency of the PML with a Geometric Conductivity Profile

Since a geometric conductivity profile has been extensively studied by Berenger, we have also considered the case of a radiating dipole located at a corner of a computational domain of $14 \times 14 \times 14$ cells, as in [8]. The electric dipole P_e was implemented by superposing to the E_z field at node (2, 2, 2) the following excitation:

$$E_{z\,ex}(n\Delta T) = -\frac{\Delta t}{\varepsilon_0 \Delta l^3}\,\frac{dP_e(n\Delta t)}{dt}$$

where

$$P_e(t) = 10^{-10}\,\exp\left(-\left(\frac{t-3T}{T}\right)^2\right)$$

with

$$T = 2 \text{ ns} \tag{23}$$

The cubic cell size Δl was 50 mm and the time step Δt was 83.333 ps. The Ez–field is observed at only two cells from the opposite corner, at point (2, 12, 2). The computational domain

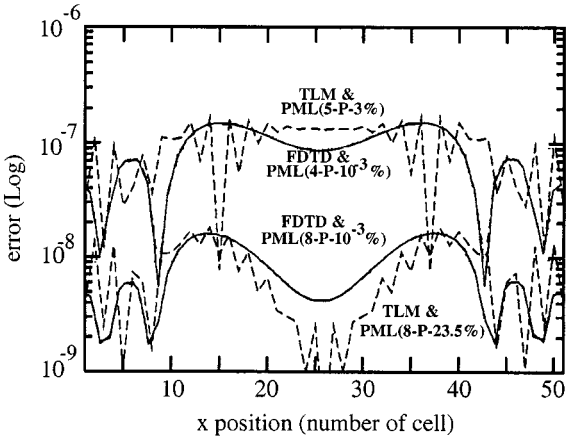

Fig. 2. Local error computed with the TLM and FDTD for various PML's using a parabolic profile.

was surrounded by $\mathrm{PML}(N\text{–}Gg\text{–}R)$. Gg means that a geometic profile of conductivity with a ratio g was used. Such a profile is implemented in the TLM using

$$\sigma(0) = -\frac{\varepsilon_0 c}{2}\frac{Ln(R)}{\Delta l}\frac{g-1}{g^N-1}$$
$$\sigma(L) = \sigma(0) g^L, \qquad \text{for } L = 1, 2, \cdots, N-1 \tag{24}$$

while in FDTD simulations, Berenger used

$$\sigma(0) = -\frac{\varepsilon_0 c}{2}\frac{Ln(R)}{\Delta l}\frac{\sqrt{g}-1}{g^N-1}$$
$$\sigma(L) = \sigma(0)\frac{g-1}{\sqrt{g}\left(\sqrt{g}-1\right)} g^L,$$
$$\text{for} \quad L = \frac{1}{2}, 1, \frac{3}{2}, 2, \cdots, N-\frac{1}{2}. \tag{25}$$

The results plotted in Fig. 3 were computed with the FDTD using $\mathrm{PML}(4\text{–}G2.15\text{–}1\%)$ and with the TLM using $\mathrm{PML}(5\text{–}G1.9-6\%)$. With such conditions, the numerical value of conductivity $\sigma(0)$ in the interface vacuum–PML is the same for both simulations ($\sigma(0) = 0.0028$ S/m). These results are very close to the corresponding reference solution calculated in a computational domain of $150 \times 150 \times 150$ cells. It can be observed that oscillations appear for both methods. According to Berenger, theses oscillations are caused by the evanescent waves, which cannot be correctly absorbed in the first cells of the PML. Consequently, oscillations can also be observed in the frequency domain. Fig. 4 shows the radiated field in the frequency domain obtained after a Fourier transform of the time responses computed up to 5000 ns. All the results are superimposed on the reference above a frequency, which is approximately 80 MHz with the FDTD and 60 MHz with the TLM. This is in accordance with the theoretical cutoff frequency bounding the domain of validity of the PML and computed in [8] using

$$f_c = \frac{\sigma(0)}{2\pi\varepsilon_0}. \tag{26}$$

In conclusion, these results show that the implementation of the PML in TLM and FDTD simulations is subject to similar numerical reflections. From our works, some guidelines for building optimal PML layers in TLM simulations can be given.

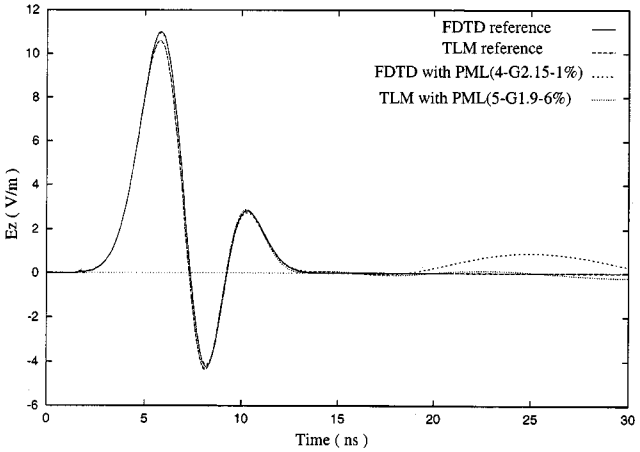

Fig. 3. Ez–field obtained in the time domain with the TLM and FDTD using a PML with a geometric profile.

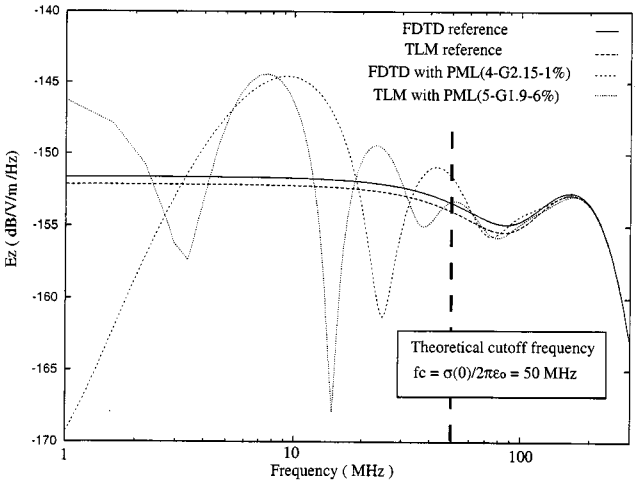

Fig. 4. Ez-field observed in the frequency domain with the TLM and FDTD using a PML with a geometric profile.

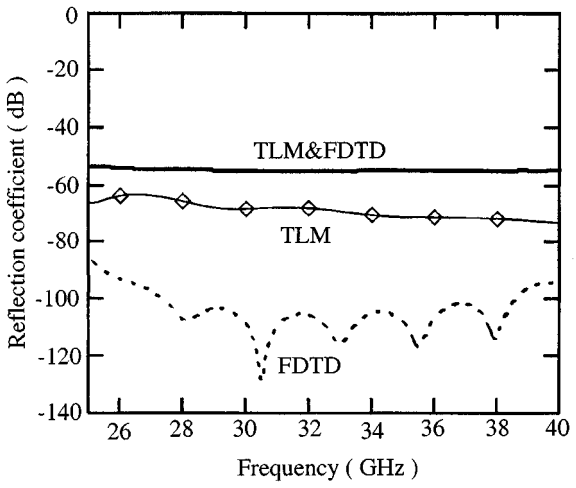

Fig. 5. Reflection error computed in a WR28 waveguide with the TLM and FDTD using PML terminations.

It is recommended to use a geometric profile of conductivity with a ratio g of approximately two in place of a parabolic

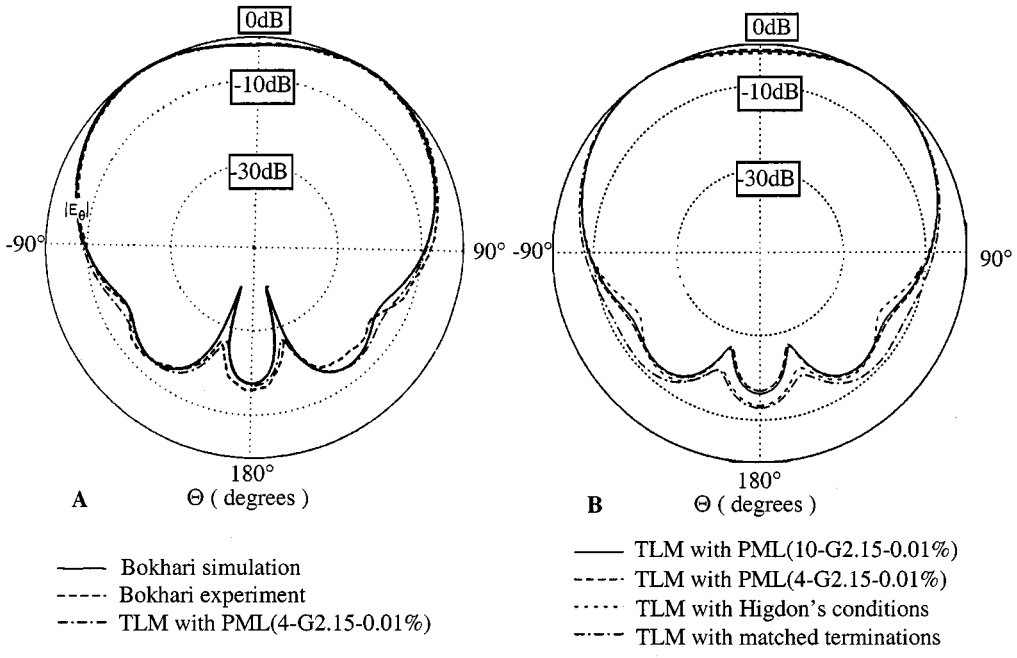

Fig. 6. Radiation patterns ($E(\theta)$ in decibels) for a microstrip patch antenna on a $1.5\lambda \times 1.5\lambda$ ground plane.

profile, which provides higher conductivity ratio. The number N of cells in the PML should be chosen in order to set the numerical value of $\sigma(0)$ in (24) according to the frequency domain of interest bounded by (26). Of course, this also depends on the theoretical reflection factor R, which are not too small for the practical purpose of stability of the algorithm. Indeed, instabilities can arise in some situations [5], as also noticed by other authors [7] for waveguide problems including discontinuities. However, we have observed that occurrence of instabilities can be sufficiently delayed in main TLM simulations by choosing $R > 0.01\%$. Futhermore, as shown with the above numerical results, a value of about 1% seems to be sufficient to obtain good absorption and, consequently, to insure stability.

IV. Applications

PML's were applied to the TLM simulation of the WR28 rectangular waveguide considered in [3]. The computational domain of $36 \times 18 \times 60$ cells was terminated at both ends with $\mathrm{PML}(25 - P - 9.10^{-13}\%)$ in order to provide $\sigma_{\max} = 25$ S/m. The dominant mode TE_{10} is generated using a Gaussian pulse (15-GHz bandwidth) modulated with a sinusoid (frequency: 32.5 GHz). The excitation plane is located at one node from one of the PML–vacuum interfaces and the output point is set one node from the opposite interface. The reflection coefficient plotted on Fig. 5 was computed using a reference solution obtained with a larger domain of $36 \times 18 \times 410$ cells terminated with $\mathrm{PML}(25 - P - 9.10^{-13}\%)$. As observed, the return loss is below -63 dB over the full operating range. These results are better than those obtained in [3] with a nonuniform TLM-FDTD mesh. However, the level of reflection is still higher with our full TLM scheme than with a full FDTD algorithm. As mentioned above, this can be explained by the higher value of $\sigma(0)$ in TLM simulation. Unfortunately, since $\sigma_{\max}$ in the PML region must be kept to an high value in order to attenuate enough the propagating waves at the end of the waveguide, it seems to not be possible to decrease $\sigma(0)$ by modifying R, as in the case of a radiating dipole in a free space. Then, for a waveguide problem, the PML with the TLM needs more cells to provide as good performance as with the FDTD.

PML's were also tested in TLM simulation of microstrip antennas. A rectangular radiated element on a finite substrate backed by a ground plane [12] was surrounded by vacuum with two cells on the sides and four cells on the top and bottom. The vacuum was then surrounded by $\mathrm{PML}(4 - G2.15 - 0.01\%)$ terminated by matched conditions. In such a situation, the complete computational domain was constituted by $51 \times 20 \times 50$ cells and the edges of the antenna were set 0.2λ from the end of the TLM network. The R factor was set to 0.01% in order to allow the results to be valid above the theoretical cutoff frequency $f_c = 2.5$ GHz. The radiation patterns were computed using the equivalence principle from the tangential E- and H-fields simulated on a rectangular surface surrounding the antenna. Thus, the output points were set one cell from the PML on the sides and three cells from the PML on the top and bottom. Fig. 6 shows the copolar radiation pattern (E_θ in the E-plane) obtained at 5 GHz. As observed in Fig. 6(a), the TLM result is very close to the theoretical and experimental data given by Bokhari in [12]. This result is also compared, in Fig. 6(b), to the radiation pattern obtained with the TLM by using an extended computational domain. In this case, the antenna was first surrounded by a three-cell vacuum and then by $\mathrm{PML}(10 - G2.15 - 0.01\%)$. This extended domain allows the edges of the antenna to be located at more than 0.8λ from the end of the TLM network. It provides a solution that can be

considered as a TLM reference solution for this problem. We have also plotted in Fig. 6(b) the radiation patterns obtained with the TLM by using the reduced domain of $51 \times 20 \times 50$ cells terminated either by Higdon's conditions or by matched terminations. We can see that the radiation pattern given by the TLM with $\mathrm{PML}(4 - G2.15 - 0.01\%)$ is superimposed on the TLM reference solution. In comparison, results given by the TLM with Higdon's conditions or matched termination differ from the reference, especially for the back radiation pattern, although the computational domain was the same.

V. Conclusion

As mentioned by Berenger for FDTD experiments, we have shown that the numerical reflections of PML's in TLM simulation are mainly subject to the numerical conductivity value implemented in the interface vacuum–PML and to the conductivity ratio from one cell to the next in the PML. As a consequence, with a correct numerical implementation of conductivity profiles in the new PML symmetrical condensed node taking into account theses two constraints, PML's provide as good performances in TLM as in FDTD simulations of open structures. It was also shown that the frequency domain of validity of the PML technique is the same for both methods. Finally, it was confirmed that the new PML symmetrical condensed node greatly improves the absorbing boundary conditions in TLM simulations of waveguides and microstrip antennas. Radiation patterns can be accurately simulated by the TLM with PML layers of four cells located at only two cells from the antenna and with a surrounding computational domain reduced to 0.2λ.

References

[1] J. P. Berenger, "A perfectly matched layer for the absorption of electromagnetic waves," *J. Comput. Phys.*, vol. 114, no. 2, pp. 110–117, Oct. 1994.

[2] C. Eswarappa and W. J. R. Hoefer, "Implementation of Berenger absorbing boundary conditions in TLM by interfacing FDTD perfectly matched layers," *Electron. Lett.*, vol. 31, no. 15, pp. 1264–1266, July 1995.

[3] N. Pena and M. M. Ney, "Absorbing-boundary conditions using perfectly matched layer (PML) technique for three-dimensional TLM simulations," *IEEE Trans. Microwave Theory Tech.*, vol. 45, pp. 1749–1755, Oct. 1997.

[4] ——, "A new TLM node for Berenger's perfectly matched layer," *IEEE Microwave Guided Wave Lett.*, vol. 6, pp. 410–412, Nov. 1996.

[5] J. L. Dubard and D. Pompei, "Simulation of Berenger's perfectly matched layer with a modified TLM node," *Proc. Inst. Elect. Eng.*, pt. H, vol. 144, pp. 205–207, June 1997.

[6] J. Paul, C. Christopoulos, and D. W. P. Thomas, "Perfectly matched layer for transmission line modeling (TLM) method," *Electron. Lett.*, vol. 33, no. 9, pp. 729–730, Apr. 1997.

[7] S. Le Maguer, N. Pena, and M. M. Ney, "Matched absorbing medium techniques for full-wave TLM simulation of microwave and millimeter-wave components," *Ann. Telecommun.*, vol. 53, no. 3–4, pp. 115–129, Mar.–Apr. 1998.

[8] J. P. Berenger, "Three-dimensional perfectly matched layer for the absorption of electromagnetic waves," *J. Comput. Phys.*, vol. 127, pp. 363–379, 1996.

[9] H. Jin and R. Vahldieck, "Direct derivations of TLM symmetrical condensed node and hybrid symmetrical condensed node from Maxwell's equations using centered differencing and averaging," *IEEE Trans. Microwave Theory Tech.*, vol. 42, pp. 2554–2561, Dec. 1994.

[10] J. C. Veihl and R. Mittra, "An efficient implementation of Berenger's perfectly matched layer (PML) for finite-difference time-domain mesh truncation," *IEEE Microwave Guided Wave Lett.*, vol. 6, pp. 94–96, Feb. 1996.

[11] J. P. Berenger, "Perfectly matched layer for the FDTD solution of wave-structure interaction problems," *IEEE Trans. Antennas Propagat.*, vol. 44, pp. 110–117, Jan. 1996.

[12] S. A. Bokhari, J. R. Mosig, and F. E. Gardiol, "Radiation pattern computation of microstrip antennas on finite ground plane," *Proc. Inst. Elect. Eng.*, pt. H, vol. 139, pp. 278–286, June 1992.

Jean-Lou Dubard was born in La Reunion, France, in 1963. He received the Ph.D. degree in electrical engineering from the Université de Nice-Sophia Antipolis, Valbonne, France, in 1992.

Since 1993, he has been an Assistant Professor at the Université de Nice-Sophia Antipolis. His research focuses on numerical modeling of microwave structures and 3-D inverse problems by using the TLM.

Dominique Pompei was born in Maillot, Algeria, in 1947. He received the Doctorat d'Etat degree from the Université de Nice-Sophia Antipolis, Valbonne, France, in 1987.

He is currently a Professor at the Université de Nice-Sophia Antipolis, where he teaches telecommunications and numerical communications. He is also Manager in the area of numerical methods of analysis for the characterization of microstrip antennas and reversal time, particularly with the TLM method.